Chapter 8
Vibration Measurement of a Rotating Structure Using an Image-Based Tracking Continuously Scanning Laser Doppler Vibrometer with a Misalignment Angle

L.F. Lyu, W.D. Zhu, D. T. Will, and K. Yuan

Abstract A novel misalignment angle correction method is developed for an image-based tracking continuously scanning laser Doppler vibrometer (CSLDV) for tracking and scanning a rotating structure with a large misalignment angle between its rotation axis and the optical axis of the tracking CSLDV's camera. In this method, the rotation trajectory of the structure is an ellipse, where the position of its center, the lengths of its semi-major axis and semi-minor axis, and the angular position of its major axis are used to determine the misalignment angle and the endpoints of the scan paths on the rotating structure. In the experimental investigation, an aluminum blade is attached to a hub on a frame, where the frame is turned to misalignment angles of 0°, 10°, 20°, and 30° between the tracking CSLDV and the rotating blade. The blade rotates at a constant speed driven by a motor inside of the hub, and the blade is excited by air flow from a fan placed behind the rotating structure. The rotating blade with different misalignment angles is tracked and scanned by the tracking CSLDV and the measured responses are processed by the improved demodulation method to estimate the modal parameters, including the damped natural frequencies and undamped mode shapes. The estimated rotation speeds and modal parameters for each angular misalignment are compared with each other, as well as to the results when angular misalignment is not considered, where the novel method is shown to produce better measurement results.

Keywords rotation tracking · misalignment angle correction

Introduction

A laser Doppler vibrometer (LDV) is a well-developed and commercialized technology for non-contact vibration measurement. The LDV can accurately measure the surface velocity of a point on a structure along the direction of its laser beam, which can then be used as the vibration response at that point [1]. To measure the responses of the structure on a measurement grid, researchers may need to use multiple LDVs or move the LDV to multiple positions, which can be expensive and time consuming. A scanning laser Doppler vibrometer (SLDV) was developed to provide measurements on a measurement grid [1–3]. In an SLDV, a scanner with a set of X- and Y-mirrors is installed in front of the LDV to reflect its laser beam. The rotation axes of the two mirrors in the scanner are orthogonal, and the rotation angles of the mirrors are considered linearly related to the horizontal and vertical position coordinates of the laser spot on the structure. The location of the laser spot can be controlled by rotating the mirrors in the scanner. The SLDV measures the responses on a measurement grid in a step scanning manner, i.e., its laser spot stays at a fixed point for a period of time and then moves to the next point [4, 5]. To increase the efficiency in measuring the vibration responses on a dense measurement grid, a continuously scanning laser Doppler vibrometer (CSLDV) was developed [6–9]. A continuous trajectory is generated on a structure and the laser spot is swept along its surface by continuously rotating the mirrors of the scanner in the CSLDV. Thus, the CSLDV can estimate mode shapes and operational deflection shapes (ODSs) with high spatial resolution. Further, to measure the three-dimensional (3D) vibration of a structure, a 3D SLDV was developed and extended to a 3D CSLDV by combining three individual CSLDVs [10–14].

L.F. Lyu · W.D. Zhu (✉) · D. T. Will · K. Yuan
Department of Mechanical Engineering University of Maryland, Baltimore County, 1000 Hilltop Circle, Baltimore, MD 21250
e-mail: linfenl1@umbc.edu; wzhu@umbc.edu; dwill1@umbc.edu; kyuan1@umbc.edu

Kristin B. Zimmerman, PhD (eds.), *Computer Vision and SLDV for Structural Dynamics, 2026, Vol. 6*, Conference Proceedings of the Society for Experimental Mechanics Series, https://doi.org/10.1007/978-8-743-81445-0_8

The CSLDV is used to measure the responses of a stationary structure under different excitations, and different operational modal analysis (OMA) methods were developed to process these measured responses. A demodulation method and a polynomial method were developed to process the measurements of a CSLDV and estimate the ODSs of a structure under sinusoidal excitation [15, 16], and the estimated ODSs were used for baseline-free damage detection [17–21]. The demodulation method was improved to allow for processing of the measured response of structures under random excitation [11, 22, 23]. A lifting method was developed to estimate the undamped modes shapes of a structure under random excitation [24–26].

To track and scan a rotating structure without attaching an encoder or mark, an edge detection image processing method with a distance condition was developed for an image-based tracking CSLDV to process the images of the rotating structure and determine its real-time position [27]. The neighboring frame subtraction technique [28] and the background subtraction technique [29] image processing algorithms were developed to improve the demodulation method so that a rotating structure with a complex background can be tracked. These image-based tracking methods do not require the tracking CSLDV to be aligned with the rotation axis of the structure being tracked. However, the estimated modal parameters of a rotating structure with a large misalignment angle between the rotation axis and the image-based tracking CSLDV can have some differences when compared to the modal parameters of a rotating structure with no misalignment angle [28]. To reduce the effects of a large misalignment angle on the estimated modal parameters of a rotating structure using the image-based tracking CSLDV, a misalignment angle correction method is needed.

The remainder of this work is as follows. A misalignment angle correction method for an image with a large misalignment angle is introduced in Sec. 2.1, a 1D scan scheme based on the misalignment angle correction method is introduced in Sec. 2.2, and a signal processing method for analyzing the measured responses is introduced in Sec. 2.3. An experimental setup for tracking and scanning a rotating blade with different misalignment angles is introduced in Sec. 3.1, misalignment angle correction results are presented in Sec. 3.2, OMA results of the rotating blade with different misalignment angles are presented in Sec. 0, and results of using the proposed method on a rotating blade in an outdoor environment are presented in Sec. 3.4. Some conclusions are presented in Sec. 4.

Methodology

Misalignment Angle Correction Method for an Image with a Large Misalignment Angle

The boundary of the trajectory of a rotating structure in its rotation plane is a circle whose radius is the radius of the rotating structure. If the boundary that can be considered as a circular object turns about a line in its radial direction, its parallel projection on the plane of the circle is an ellipse (Figure 1), where the lengths of its semi-major axis and semi-minor axis are a and b, respectively. Figure 1 depicts the top and front views of both the original circular object and the turned circular object. The turning angle of the circular object can be calculated by

$$\theta = \arccos(b/a) \tag{1}$$

In this research, the boundary of the trajectory of the rotating blades, whose hub is mounted on an aluminum frame, is considered as a circular object (Figure 2). The trajectory of the rotating blades shown in Figure 2(b) is an overlay of 500 images of the rotating blades captured by the camera in an image-based tracking CSLDV with a constant frame rate of 25 frames per second. When the rotation axis of the rotating blades is aligned with the optical axis of the camera, the boundary of the trajectory is a circle and Eq. (1) can be used to find that $\theta = 0°$.

When the rotation axis of the rotating blades is not aligned with the optical axis of the camera, the boundary of the trajectory of the rotating blades in the captured images is considered as an ellipse (Figure 3), where the frame supporting the rotating blades is turned 30°. The parameters of the ellipse shown in Figure 3 are determined by the ellipse detection algorithm in Ref. [30], where the pixel coordinates of the ellipse center are (571.26, 508.62), the lengths of the semi-major axis and semi-minor axis are 455.99 pixels and 399.16 pixels, respectively, and the angle between the semi-major axis and the X-axis is −88.47°. Using Eq. (1), the calculated angle between the rotation axis of the blades and the optical axis of the camera is 28.91°.

The parameters of the ellipse can be used to generate an accurate scan path on a rotating blade with a large misalignment angle of 30°. To generate a scan path on the rotating blade, the first step is to determine the position of the rotating blade in a captured image from the camera. In this work, the distance condition in Ref. [28] and the background averaging technique in Ref. [29] are used to determine the position of an edge point of the rotating blade. The details of the image processing method for tracking the rotating blade can be found in Ref. [27–29].

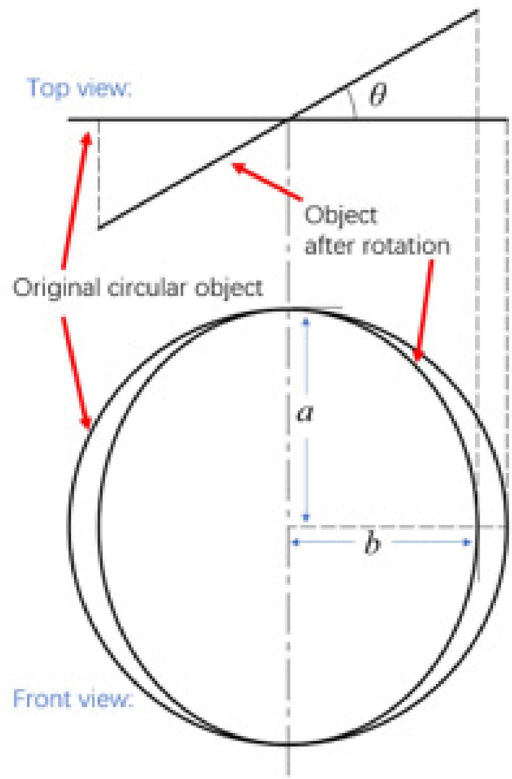

Fig. 1 Schematic of the parallel projection of the rotated circular object.

(a) (b)

Fig. 2 (a) Image of the rotating blades, and (b) the image of the trajectory of the rotating blades in (a).

In Figure 4, the middle line of the rotating blade is considered as a line passing through its rotation center, and the angle between the middle line and the X-axis is determined by the position of the edge point and the angle α. The equation of the middle line is given by

$$(y-n) = (x-m)\tan\beta \tag{2}$$

where (m, n) are the coordinates of the rotation center, and β is the angle between the middle line and the X-axis. The equation of the ellipse is given by

$$\frac{[(x-p)\cos\varphi+(y-q)\sin\varphi]^2}{a^2}+\frac{[(p-x)\sin\varphi+(y-q)\cos\varphi]^2}{b^2}=1 \tag{3}$$

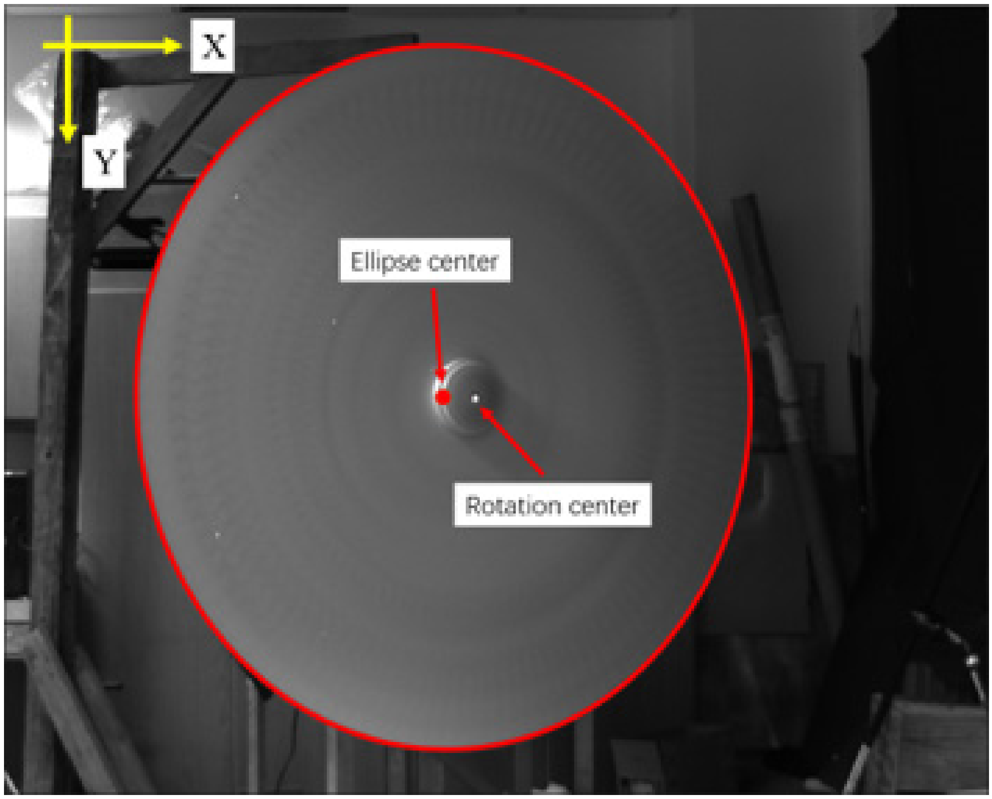

Fig. 3 Image of the trajectory of the rotating blades with its estimated boundary.

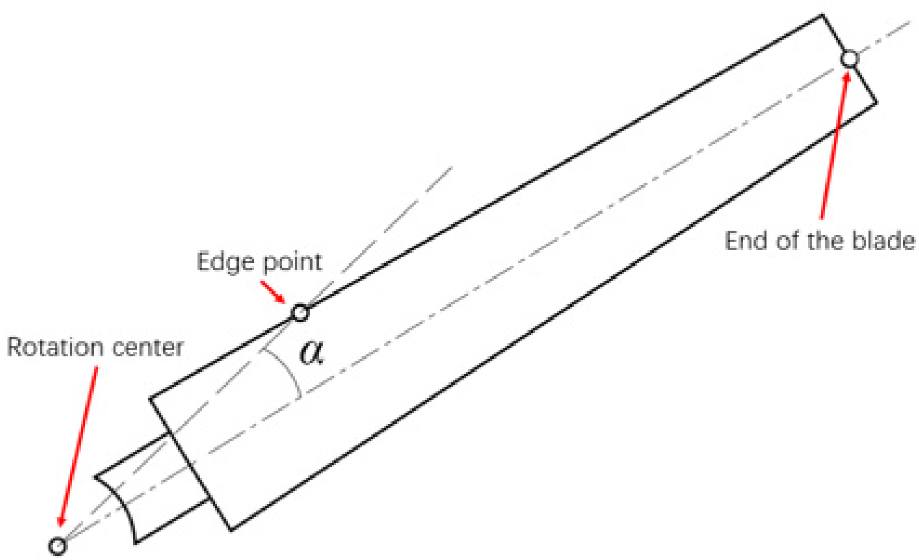

Fig. 4 Schematic of the rotating blade.

where (p, q) are the coordinates of the ellipse center, and φ is the angle between the major axis of the ellipse and the X-axis (Figure 5). The intersection point of the ellipse and the middle line is the end of the rotating blade, and its position is used to generate accurate scan paths on the rotating blade. Eq. (2) can be rewritten as

$$\begin{cases} x = m + t\cos\beta \\ y = n + t\sin\beta \end{cases} \tag{4}$$

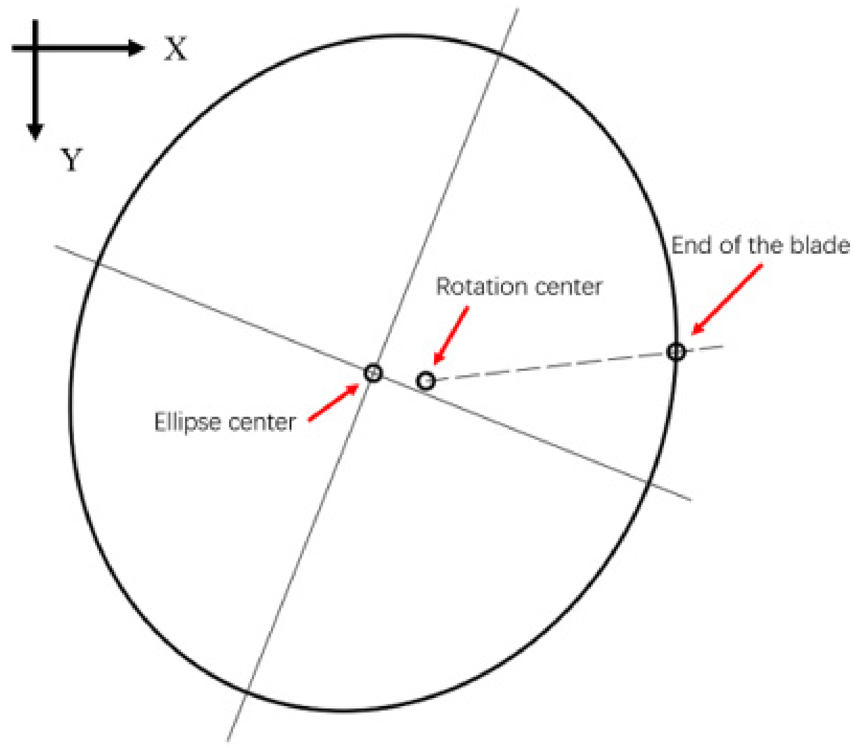

Fig. 5 Schematic of the trajectory boundary of the rotating blade with a large misalignment angle.

where *t* is a positive parameter. Substituting Eq. (4) into Eq. (3) yields

$$\frac{[(m+t\cos\beta-p)\cos\varphi+(n+t\sin\beta-q)\sin\varphi]^2}{a^2}+\frac{[(p-m-t\cos\beta)\sin\varphi+(n+t\sin\beta-q)\cos\varphi]^2}{b^2}=1 \quad (5)$$

Eq. (5) can be derived as

$$At^2+Bt+C=0 \quad (6)$$

where $A=\frac{\cos^2(\beta-\varphi)}{a^2}+\frac{\sin^2(\beta-\varphi)}{b^2}$, $B=\frac{2\cos(\beta-\varphi)[(m-p)\cos\varphi+(n-q)\sin\varphi]}{a^2}-\frac{2\sin(\beta-\varphi)[(p-m)\sin\varphi+(n-q)\cos\varphi]}{b^2}$, and $C=\frac{[(m-p)\cos\varphi+(n-q)\sin\varphi]^2}{a^2}+\frac{[(p-m)\sin\varphi+(n-q)\cos\varphi]^2}{b^2}-1$. The solutions to Eq. (6) are $t_1=\frac{-\text{B}+\sqrt{B^2-4AC}}{2A}$ and $t_2=\frac{-\text{B}-\sqrt{B^2-4AC}}{2A}$, where t_1 is chosen to be substituted into Eq. (4) since $t>0$. Once the position of the intersection point is obtained, it can be used to generate the endpoints of a scan path on the rotating structure.

1D Scan Scheme

Let the estimated position of the end of the rotating blade be (x_{end}, y_{end}). The position of an endpoint of the scan path on the rotating blade can be calculated by

$$\begin{cases} x=m+c(x_{\text{end}}-m) \\ y=n+c(y_{\text{end}}-n) \end{cases} \quad (7)$$

where c is a coefficient. By changing the value of c, the endpoint near the hub of the rotating blade and the endpoint near the free end of the rotating blade can be generated. The generated endpoints are shown in Figure 6(a), where 20 endpoints are generated near the boundary of the trajectory of the rotating blades and 20 endpoints are generated near the hub of the rotating blades. Using the misalignment angle correction method and considering the misalignment angle, the scan paths are generated based on the position coordinates of the endpoints and 100 scan paths are shown in Figure 6(b) as dashed lines. Conversely, if the legacy method is used where the misalignment angle is not considered when generating the scan paths [28], the scan paths may not align with the trajectory of the rotating blades (Figure 6(c)). The scan paths shown in Figure 6(c) are generated by the angular position of the middle line of the rotating blade only, and the boundary of the scan paths is a circle. As shown in Figure 6(c), portions of some scan paths are outside of the boundary of the trajectory of the rotating blades, which will add noise to the measurements of the image-based tracking CSLDV. Further, if the scan paths are

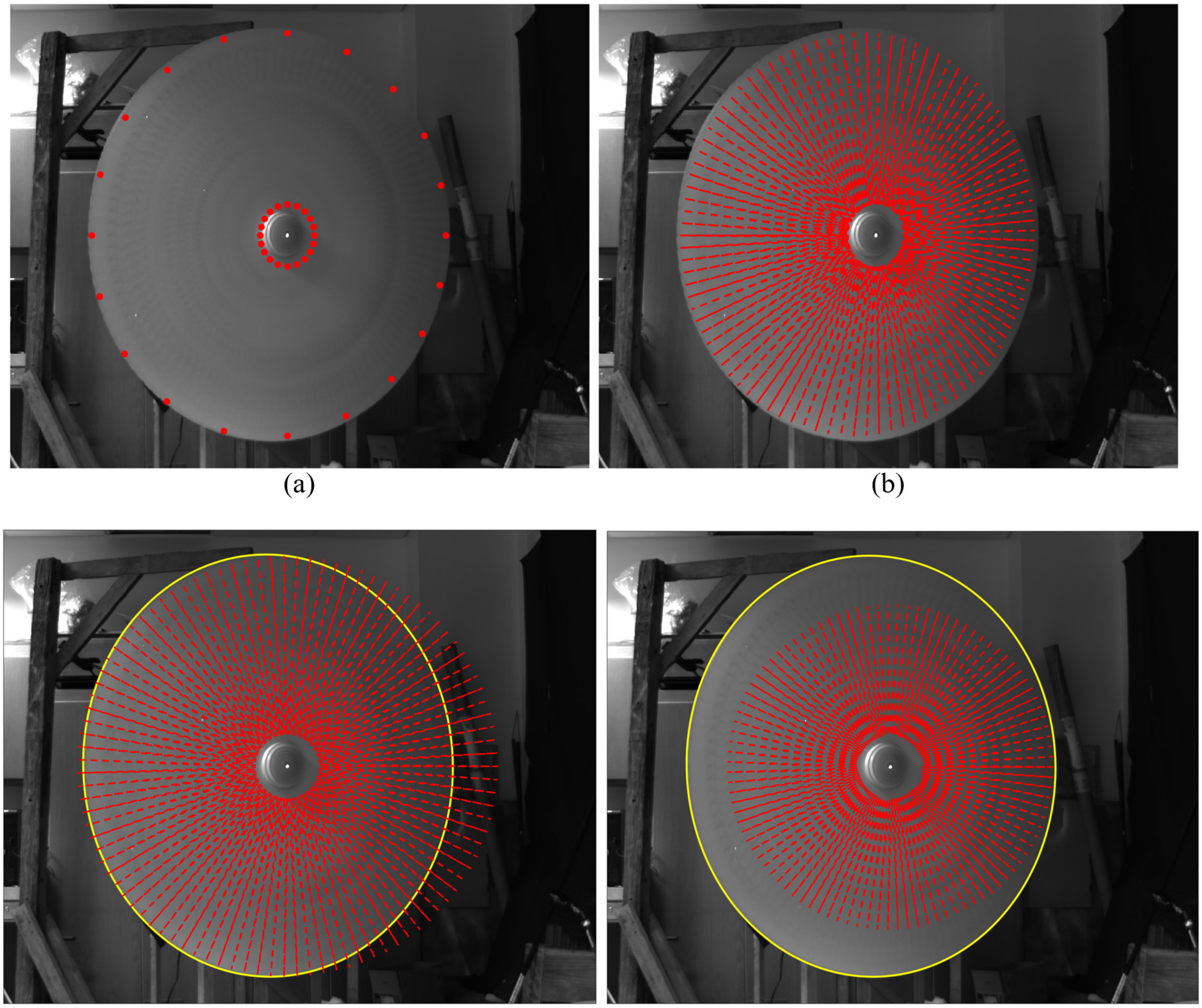

(a) (b) (c) (d)

Fig. 6 (a) Endpoints of the scan paths generated on the trajectory of the rotating blades, (b) the scan paths generated on the trajectory of the rotating blades based on the estimated position coordinates of the end of the rotating blade, (c) the scan paths generated on the trajectory of the rotating blades based on the angular position of the middle line of the rotating blade, and (d) the shortened scan paths in (c).

shortened such that they are within the boundary of the trajectory of the rotating blades, the scan paths cannot fully capture the entire trajectory of the rotating blades (Fig. 6(d)), leading to inaccurate OMA results.

Signal Processing Methods for Image-Based Tracking CSLDV Measurements

The position of the shifted edge point on the middle line of the rotating blade can be used to calculate the rotation speed of the blade. To increase the accuracy of the estimated rotation speed, the middle line on the elliptical trajectory of the rotating blade can be transformed to the middle line on the original circular trajectory. The solid elliptical boundary line and the dashed circular boundary line are shown in Fig. 7(a), where the major axis of the ellipse is considered the radial direction at which the original circular boundary rotates about. In Fig. 7(b), point *O* is the ellipse center, points *A* and *B* are two estimated positions of the end of the rotating blade from two neighboring frames captured by the camera, and points *A'* and *B'* are points on the original circular boundary that correspond to points *A* and *B*, respectively. The line passing through points *A* and *A'* and the line passing through points *B* and *B'* are perpendicular to the major axis of the elliptical boundary. Let the angle between line *OA* and the X-axis be β_A, and the angle between line *OA* and the major axis of the ellipse is $\beta_A - \varphi$. The

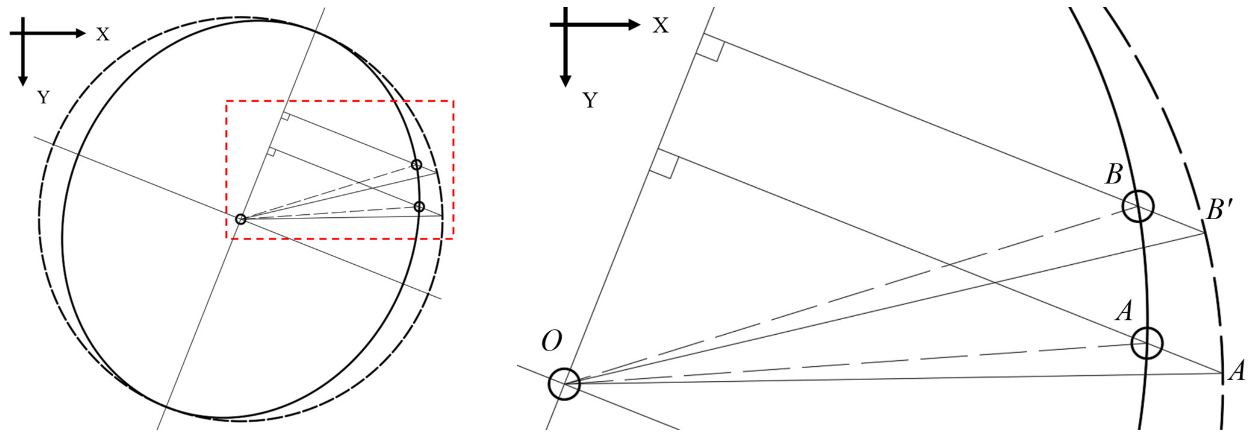

Fig. 7 (a) Schematic of the elliptical boundary and the circular boundary, and (b) a zoomed-in view of the schematic showing the transformation of the ends of the rotating blade on the elliptical boundary to the circular boundary.

angle between line *OA'* and the X-axis is

$$\beta_{A'} = \arctan\left[\frac{a}{b}\tan\left(\beta_A - \varphi\right)\right] + \varphi \tag{8}$$

Let the angle between line *OB* and the X-axis be β_B, and the angle, $\beta_{B'}$, between line OB' and the X-axis can be calculated using Eq. (8) by substituting in β_B and $\beta_{B'}$. The angle $\angle B'OA' = \beta_{A'} - \beta_{B'}$ is the angle between the two middle lines on the original circular trajectory, which is considered as the real angular movement of the rotating blade during the time period T between the two neighboring frames captured by the camera. The rotation speed of the blade in revolutions per minute (rpm) is

$$R = \frac{30(\beta_{A'} - \beta_{B'})}{\pi T} \tag{9}$$

Note that the ellipse center is not the rotation center due to the perspective projection (Figure 3), so the angles obtained by the transformation in Eq. (8) are approximations of the actual angles. These approximated angles are subsequently used to calculate the rotation speed of the blade in this work. In previous research, the rotation speed was calculated using the angle $\angle BOA$ [28], which is different from the rotation speed that is calculated when using the angle $\angle B'OA'$, and this is discussed in Sec. 3.2.

The improved demodulation method is used for OMA of the measured responses of the rotating blade [22]. For estimating the end-to-end undamped mode shapes of the rotating blade, square roots of the sum of squares of the X- and Y-mirror signals are calculated and used as position coordinates of the laser spot on a scan path during scanning of the rotating blade [22]. The measured responses are filtered by a band-pass filter that only contains one damped natural frequency of the rotating blade. The filtered responses are first multiplied by sinusoidal signals whose frequencies are the damped natural frequency, and then the responses are filtered by a low-pass filter to estimate the undamped mode shape corresponding to the damped natural frequency.

Experimental Investigation

Experimental Setup

In this work, an image-based long-range tracking CSLDV developed in Ref. [29] was used for tracking and scanning a rotating blade. The image-based long-range tracking CSLDV consists of a Polytec RSV-150 remote sensing vibrometer, a Cambridge 6240H scanner, and a Basler acA1300-200um camera (Figure 8(a)). The scanner has a set of X- and Y-mirrors that are connected to two stepper motors, and the rotation axes of the motors are perpendicular to each other. The image-based long-range tracking CSLDV is connected to an NI controller that generates input signals to the scanner and receives the measured responses and feedback signals from the scanner. One of the three aluminum blades, with a width of 0.1 m

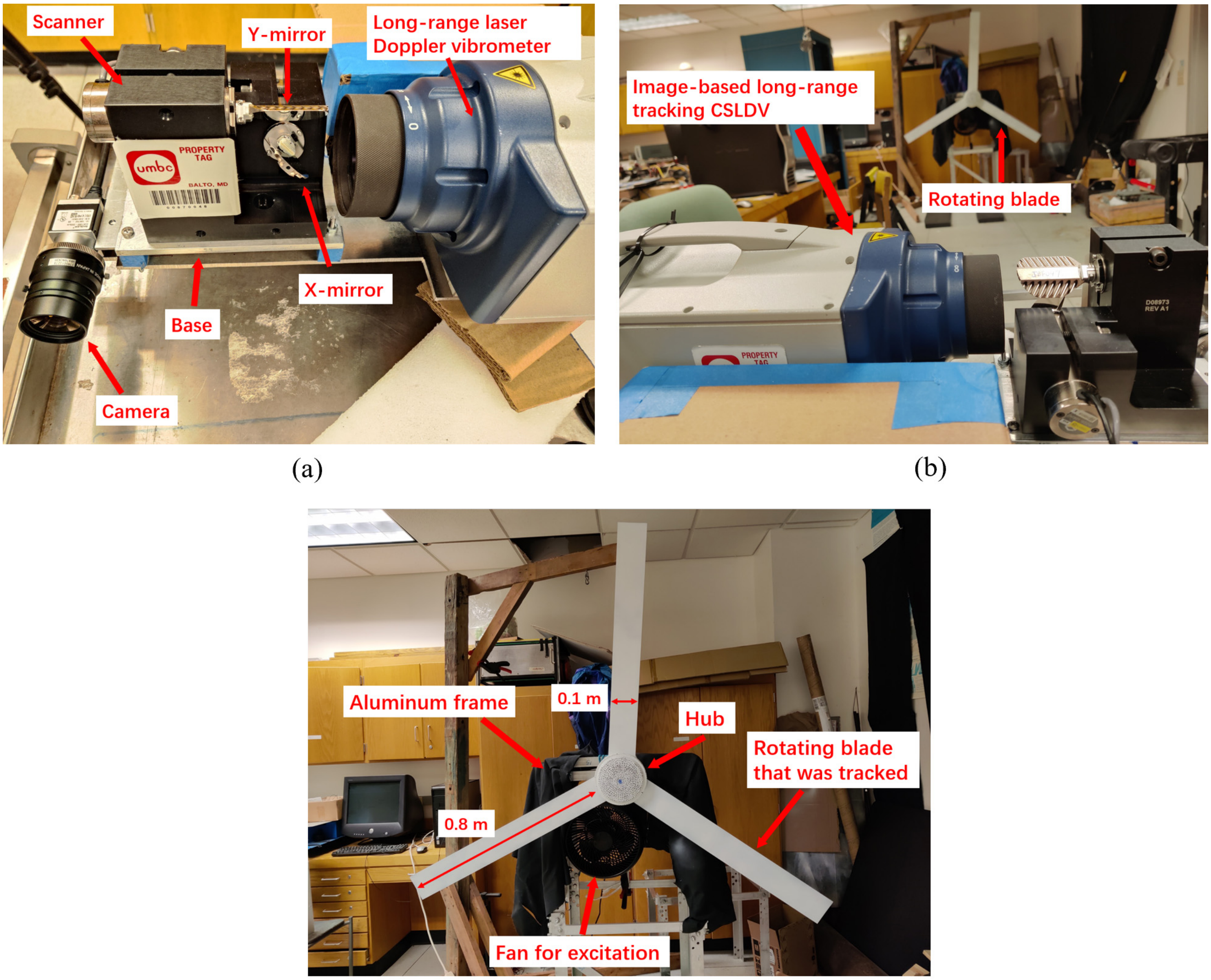

(a) (b)

(c)

Fig. 8 (a) Photograph of the image-based long-range tracking CSLDV, (b) the experimental setup involving the tracking and scanning of the rotating blade with the image-based long-range tracking CSLDV, and (c) a photograph showing the rotating blade that was tracked.

and a length of 0.8 m, that were attached to a hub was tracked by the camera (Figure 8(b)). The hub was mounted on an aluminum frame, and the hub rotated with a constant speed when the internal motor was switched on (Figure 8(c)).

For the investigation of tracking and scanning a rotating blade with a misalignment angle between its rotation axis and the optical axis of the camera, the aluminum frame was turned at different positions so that there were different misalignment angles of 0°, 10°, 20°, and 30° between the tracking CSLDV and the rotating blade. The blade rotated with a constant speed for different misalignment angles, and the camera captured images of the rotating blade with a frame rate of 25 frames per second. Air flow from a separate fan positioned behind the rotating blades was used to excite the rotating blades. The distance between the center of the hub and the image-based long-range tracking CSLDV was 5.07 m with no misalignment angle, and the distance was 5.16 m with a misalignment angle of 30°.

Misalignment Angle Correction Method Results with Different Misalignment Angles

Captured images of the rotating blade with different misalignment angles are shown in Figure 9, where the image with no misalignment angle is shown in Figure 9(a) and images with misalignment angles of 10°, 20°, and 30° are shown in Figure 9(b), (c), and (d), respectively. Rotation trajectories of the blade with different misalignment angles are shown in

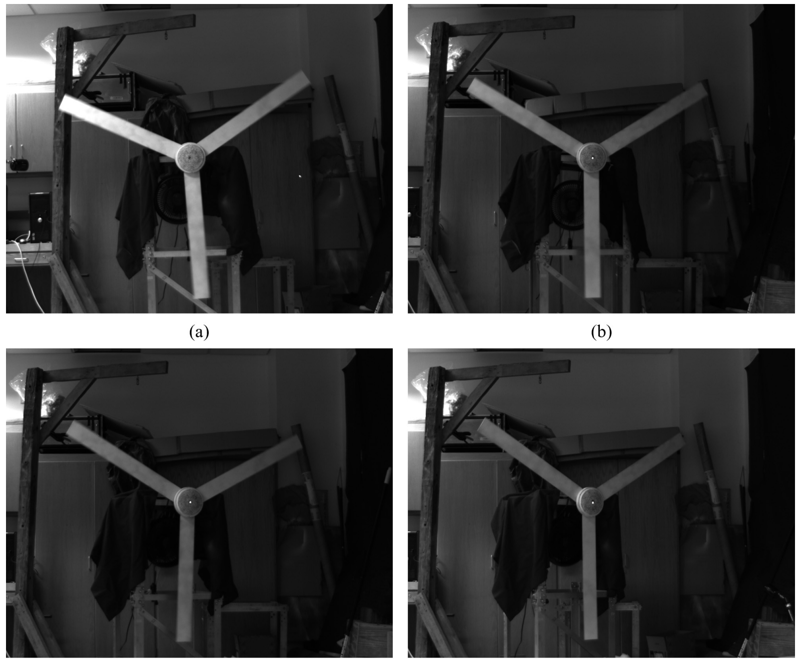

(a) (b) (c) (d)

Fig. 9 Captured images of the rotating blade with (a) no misalignment angle, (b) a misalignment angle of 10°, (c) a misalignment angle of 20°, and (d) a misalignment angle of 30°.

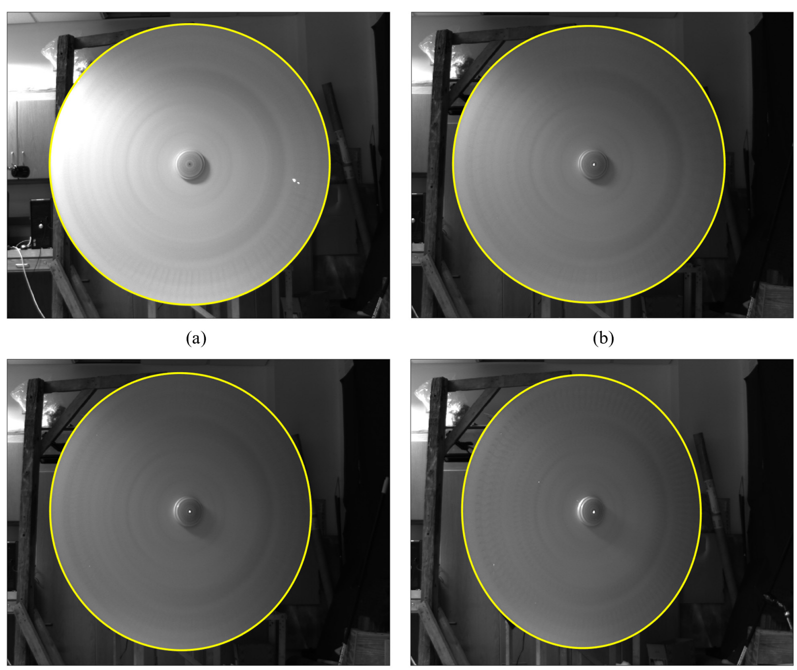

(a) (b) (c) (d)

Fig. 10 Trajectories of the rotating blade with (a) no misalignment angle, (b) a misalignment angle of 10°, (c) a misalignment angle of 20°, and (d) a misalignment angle of 30°.

Figure 10, where each trajectory is an overlay of 500 images captured by the camera while the blade rotated with a constant speed. The boundaries of the rotation trajectories were identified as ellipses using the ellipse detection algorithm given in Ref. [30], and the parameters of the ellipses shown in Figure 10 are presented in Table 1. Note that the lengths of the major

Table 1 Estimated parameters of the elliptical boundaries of the trajectories of the rotating blade with different misalignment angles.

Misalignment Angle	*a* (pixels)	*b* (pixels)	(*p*, *q*) (pixels)	φ	θ
0°	468.61	468.44	(610.57, 509.20)	−88.54°	1.54°
10°	462.48	455.09	(594.62, 509.34)	−88.51°	10.26°
20°	462.91	436.12	(579.99, 509.57)	−88.51°	19.59°
30°	455.99	399.16	(571.26, 508.62)	−88.47°	28.91°

axis and minor axis of the ellipse in Figure 10(a) are approximately the same, meaning that the boundary is close to a circle with no misalignment angle. The angles, θ, between the rotation axis and the optical axis of the camera were calculated using Eq. (1). The rotation plane of the blade was approximately perpendicular to the ground and the aluminum frame was turned about the vertical direction. Therefore, the major axes of the resulting elliptical boundaries shown in Figure 10 are approximately vertical. Thus, the calculated angles, φ, between the major axes of the ellipses and the X-axis given in Table 1 are close to −90°.

The background averaging method described in Ref. [29] was used to process the captured images from the camera, and the processing of Figure 9(d) is presented here as an example. The averaged image using 500 captured images for the case with a misalignment angle of 30° is shown in Figure 11(a). To remove the background from the scene, the averaged image was subtracted from a captured image, such as the image shown in Figure 9(d). In the resulting image, the three blades remain and the background is removed, as shown in Figure 11(b). The Canny edge detection method was applied

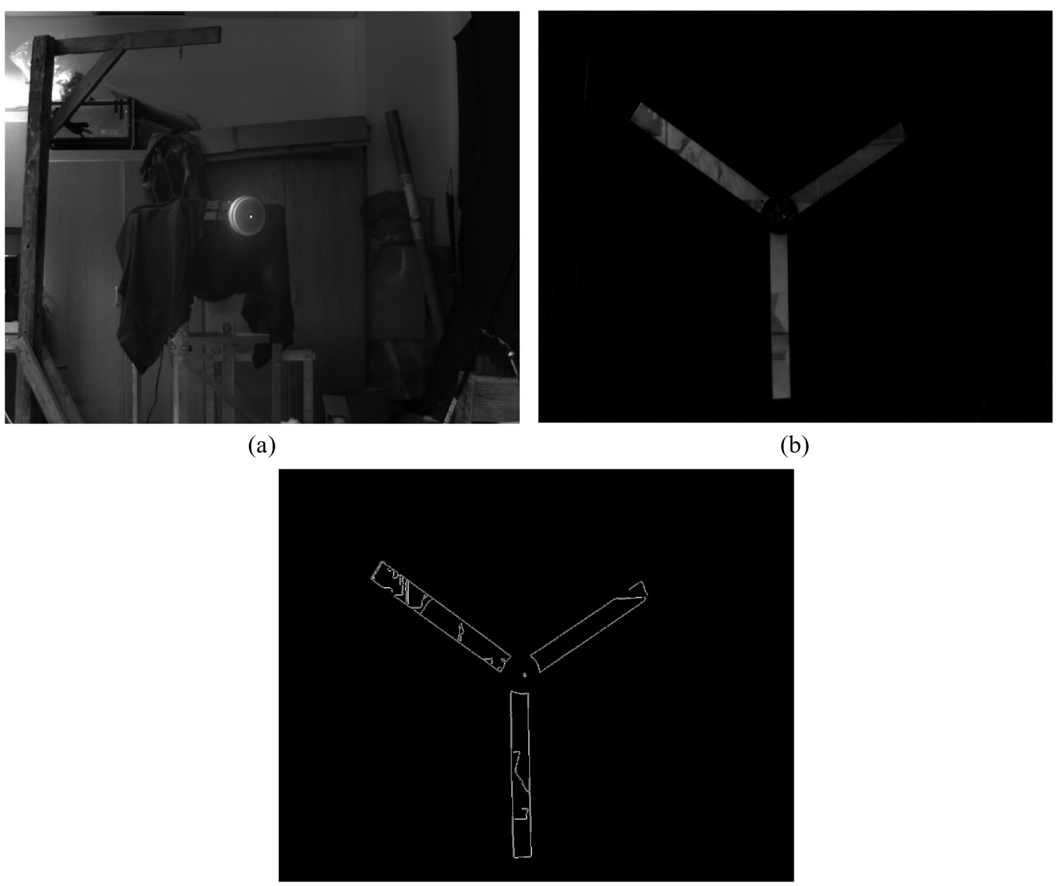

(a) (b) (c)

Fig. 11 (a) Averaged image using 500 captured images for the case with a misalignment angle of 30°, (b) the resulting image obtained by subtracting the averaged image from the captured image shown in Figure 9(d), and (c) the edge map obtained by applying the Canny edge detection method to (b).

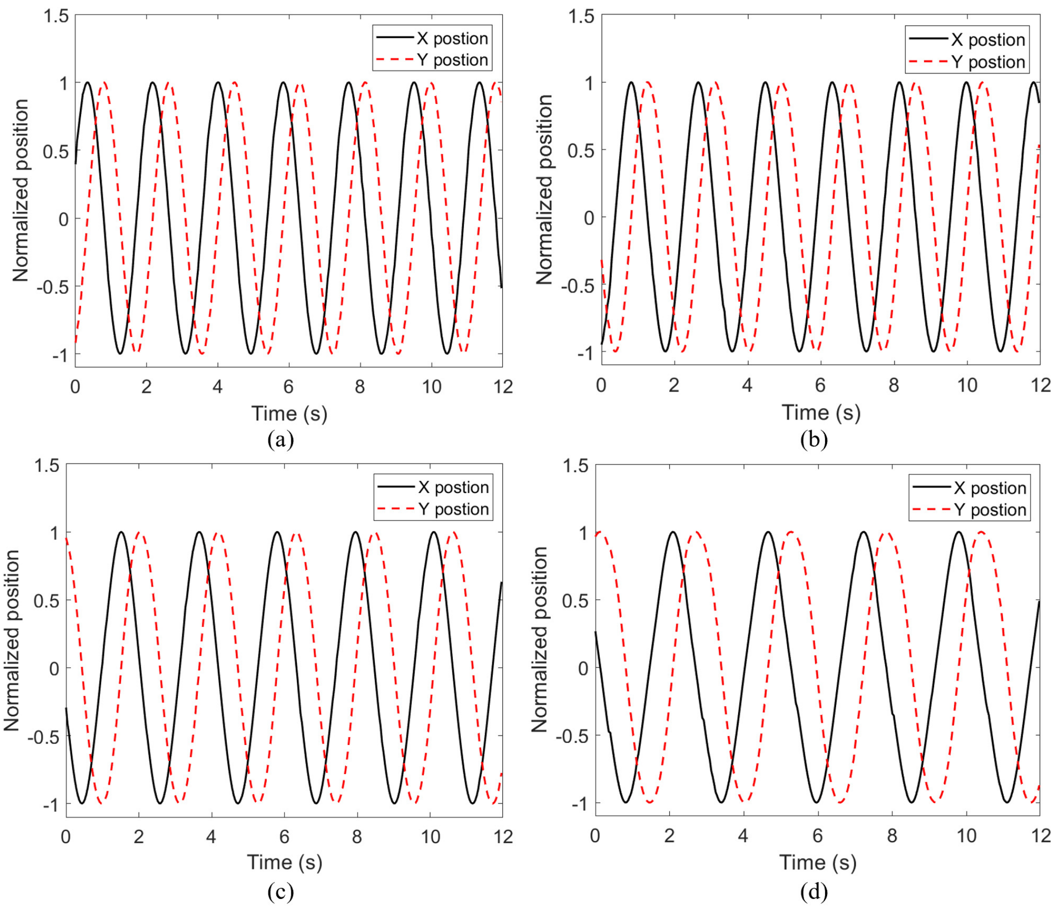

Fig. 12 Normalized position coordinates of the edge point with (a) no misalignment angle, (b) a misalignment angle of 10°, (c) a misalignment angle of 20°, and (d) a misalignment angle of 30°.

to Figure 11(b) and the resulting edge map is shown in Figure 11(c), where the edges of the three blades are depicted. For tracking one of the three rotating blades, the distance condition described in Ref. [27] was used to determine the position of an edge point on the rotating blade.

The normalized estimated position coordinates of the edge point of the rotating blade are shown in Figure 12 for each misalignment angle case, where the position coordinates of the rotation center were subtracted from the estimated position coordinates of the edge point and the resulting position coordinates were normalized by dividing by their maximum values. The estimated position coordinates were processed by using the novel method described in Sec. 2.3, where the elliptical trajectory was transformed to the circular trajectory to obtain the estimated rotation speeds of the blade at different misalignment angles. The estimated rotation speeds of the blade at different misalignment angles are shown in Figure 13. The averages of the estimated rotation speeds for each misalignment angle case shown in Figure 13 are given in Table 2, where the percent errors between the average rotation speeds with angular misalignments (10°, 20°, 30°) and the average rotation speed with no angular misalignment (0°) are calculated using the equation, $\%\, error = \frac{approximate\ value - true\ value}{true\ value} \times 100$, where the "true value" is taken as the case with no misalignment angle and the non-zero misalignment angle cases are taken as the "approximate values". For the misalignment angle of 30°, the average value of the rotation speed calculated using the legacy method is 32.78 rpm which is nearly identical to the average rotation speed of 32.79 rpm calculated using the novel method, as shown in Table 2.

OMA Results with Different Misalignment Angles

The damped natural frequencies of the rotating blade with different misalignment angles were estimated from fast Fourier transform (FFT) results of the measured responses of the rotating blade [29], and they are given in Table 3. The relative percent error between the case of no misalignment angle and the non-zero misalignment angle cases is given in Table 3.

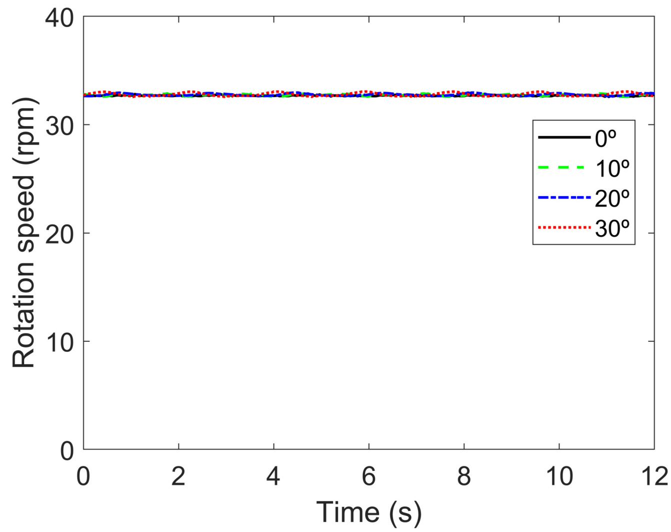

Fig. 13 Estimated rotation speeds of the blade processed using the novel method described in Sec. 2.3.

Table 2 Estimated averaged rotation speeds calculated using the novel method for different misalignment angles as well as their corresponding percentage errors.

Misalignment Angle	Average Rotation Speed (rpm)	Percent Error (%)
0°	32.68	——
10°	32.74	0.18
20°	32.77	0.28
30°	32.79	0.34

Table 3 Estimated damped natural frequencies of the rotating blade with different misalignment angles as well as their corresponding percentage errors.

Misalignment Angle	First Damped Natural Frequency (Hz)	Second Damped Natural Frequency (Hz)	Third Damped Natural Frequency (Hz)	% Error First Mode (%)	% Error % Second Mode (%)	% Error Third Mode (%)
0°	1.631	9.248	29.655	-	-	-
10°	1.655	9.269	29.887	1.47	0.23	0.78
20°	1.642	9.292	29.821	0.67	0.48	0.56
30°	1.635	9.233	29.372	0.24	-0.16	-0.96
30° without considering projection	1.646	9.295	29.434	0.92	0.51	-0.75

Note that the differences between the damped natural frequencies of the rotating blade with no misalignment angle and those with a misalignment angle are relatively small, with a maximum percent error of 1.47%. If the laser spot is swept over the surface of the rotating blade, its damped natural frequencies can be accurately estimated, independent of the tracking and scanning method used.

The first three undamped mode shapes of the rotating blade were estimated using the improved demodulation method. The estimated undamped mode shapes of the rotating blade with different misalignment angles, where the rotation speed was calculated using the novel method that considers projection in the captured images from the camera, are shown in Figure 14. These mode shapes are out-of-plane bending mode shapes of a rotating beam, and the results show that there is good agreement of the mode shapes between each angular misalignment case. The undamped mode shapes of the rotating blade with a misalignment angle of 30° were estimated using both the novel and legacy methods as shown in Figure 15. Modal assurance criterion (MAC) values between the undamped mode shapes with no misalignment angle and the undamped mode shapes with different misalignment angles are shown in Table 4. The MAC values between the estimated undamped mode shapes with no misalignment angle and those with non-zero misalignment angles calculated using the novel method that considers projection are very high (0.97 or greater), while the MAC values between the estimated undamped mode shapes with no misalignment angle and those with the misalignment angle of 30° calculated using the legacy method that does not

Table 4 MAC values between the estimated undamped mode shapes of the rotating blade with no misalignment angle and the estimated undamped mode shapes with different misalignment angles.

Angular Misalignment	First Mode	Second Mode	Third Mode
10°	0.99	0.99	0.97
20°	0.99	0.98	0.97
30°	0.99	0.99	0.97
30° without considering projection	0.99	0.94	0.89

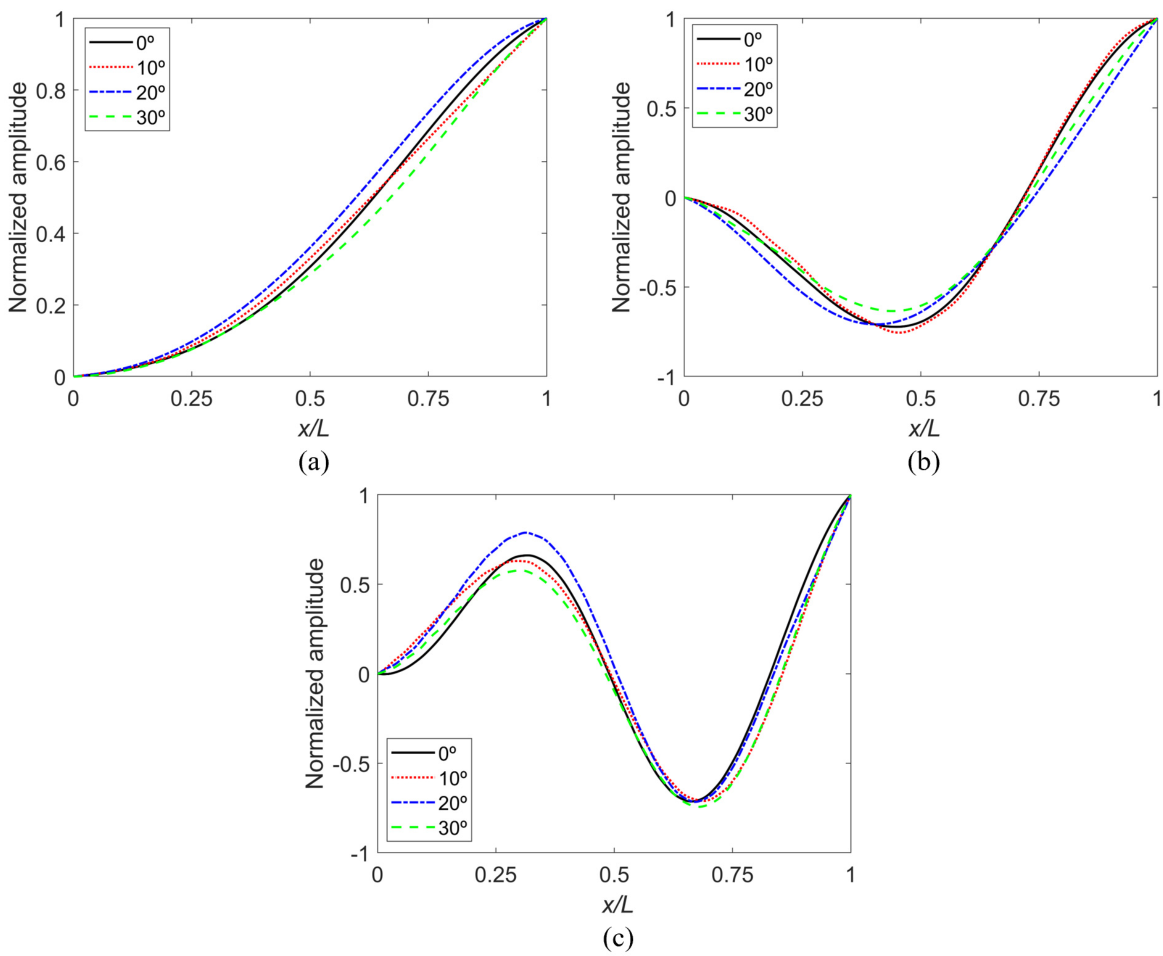

Fig. 14 Estimated (a) first, (b) second, and (c) third undamped mode shapes of the rotating blade with different misalignment angles calculated using the novel method described in Sec. 2.3.

consider projection have lower values for the second and third modes (0.94 and 0.89, respectively). Using the novel method that considers projection in the captured images can greatly reduce differences in the estimated undamped mode shapes caused by angular misalignments between the rotation axis and the optical axis of the camera.

Application of the Proposed Method on Tracking the Rotating Blade in an Outdoor Environment

In this section, the proposed method was experimentally validated through an outdoor test. As shown in Fig 16(a), the frame was moved outside the lab environment, and the motor in the hub was connected to a portable power station so that it could be switched on and rotate with a constant speed. The trajectory of the rotating blades with its boundary is shown in Figure 16(b). The semi-major axis and semi-minor axis of the boundary are 299.4 pixels and 298.9 pixels, respectively. Using Eq. (1), the misalignment angle between the rotation axis of the blades and the optical axis of the camera is 3.3°.

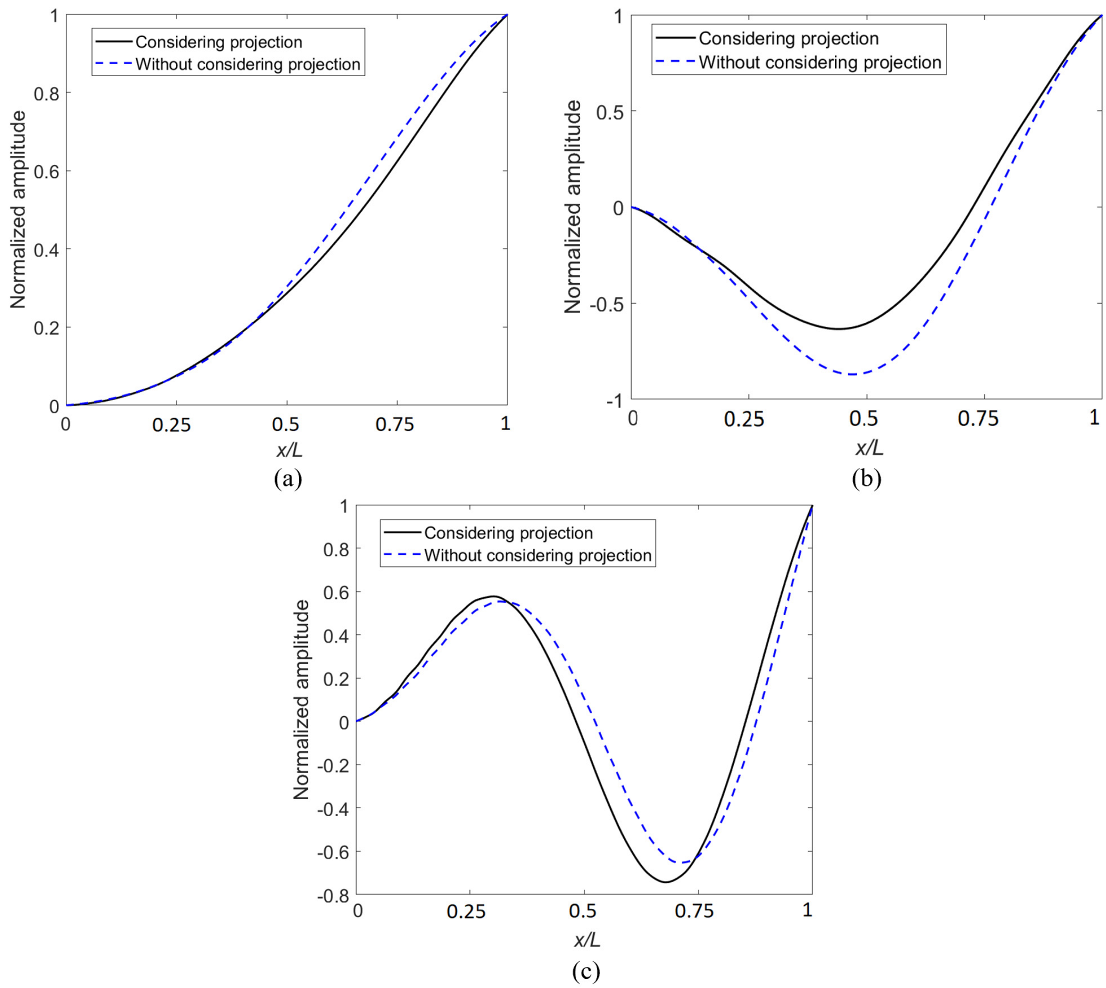

Fig. 15 Estimated (a) first, (b) second, and (c) third undamped mode shapes of the rotating blade with a misalignment angle of 30° using the novel misalignment angle correction method that considers projection and the legacy method that does not consider projection.

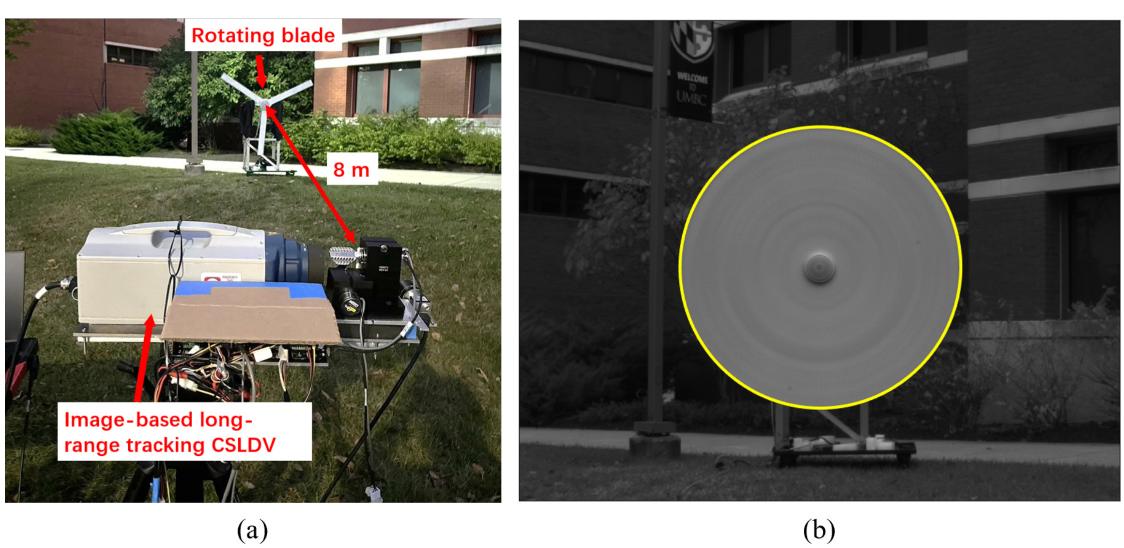

Fig. 16 (a) Experimental setup of the outdoor test for validating the proposed method of tracking and scanning a rotating blade, and (b) the estimated boundary of the trajectory of the rotating blades.

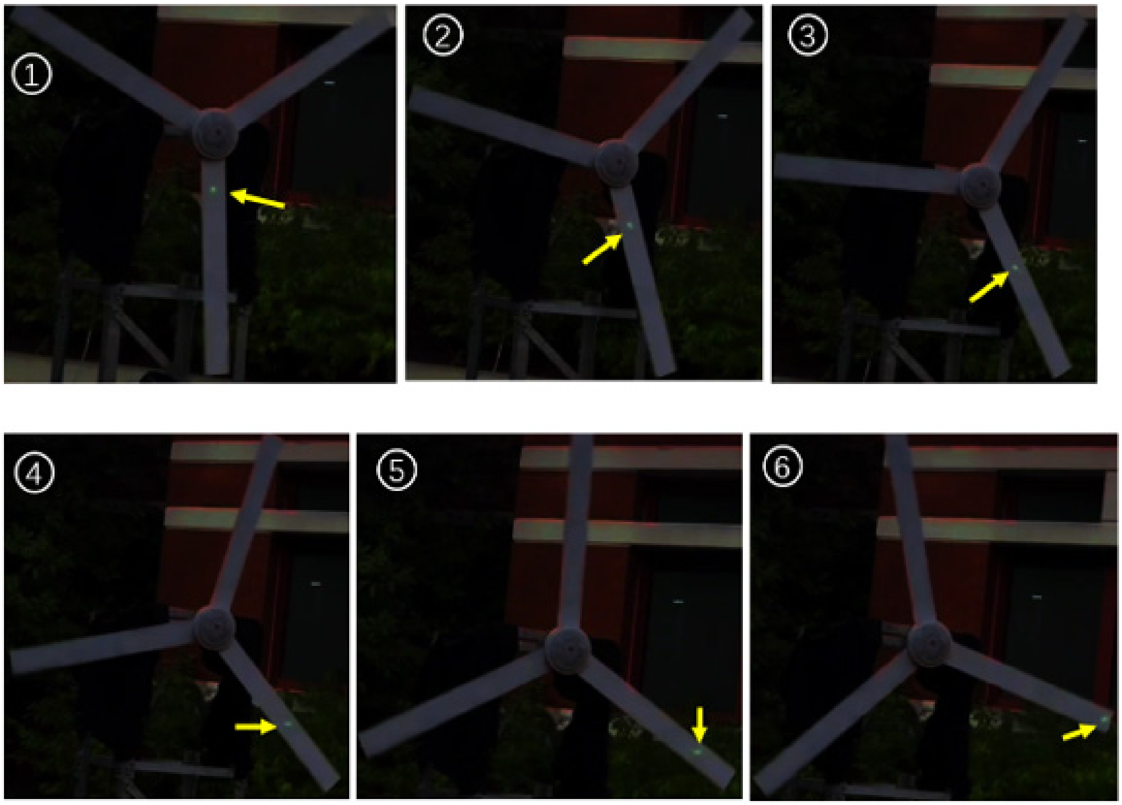

Fig. 17 Series of frames captured by the camera showing the location of the laser spot along its scan path as the blade rotated.

Straight scan paths were generated along the direction of the middle line of the rotating blade based on the pixel positions of the edge point. A series of six frames captured by the camera in the image-based long-range tracking CSLDV are shown in Figure 17, where the locations of the laser spot are indicated by arrows. Note that the frames shown in Figure 17 were processed to increase the contrast between the laser spots and the other objects in the frames. In the series of frames, the laser spot is moved along the middle line of the rotating blade, which is its generated scan path used for capturing vibration data of the rotating structure.

Conclusion

A novel misalignment angle correction method was developed for processing images of a rotating structure with a large misalignment angle between its rotation axis and the optical axis of the camera that captured its images. The rotation trajectory of the structure is considered as an ellipse due to the projection in the captured images from the camera. Parameters of the ellipse, including the position of its center, the lengths of its semi-major axis and semi-minor axis, and the angular position of its major axis, are used to determine the misalignment angle and the endpoints of the scan paths on the rotating structure. The difference between the center of the ellipse and the rotation center of the structure is considered in the misalignment angle correction method to determine accurate position coordinates of the rotating structure in the captured images. The estimated position coordinates of the end of the rotating structure in the elliptical trajectory are transformed into position coordinates in the original circular rotation trajectory to obtain the estimated rotation speeds of the blade at different misalignment angles.

An aluminum blade attached to a hub was used as a rotating structure for the experimental investigation of the misalignment angle correction method. The rotating blade with different misalignment angles of 0°, 10°, 20°, and 30° was tracked and scanned by the tracking CSLDV and its modal parameters, including the damped natural frequencies and undamped mode shapes, were estimated by the improved demodulation method. The estimated damped natural frequencies of the rotating blade with different misalignment angles matched well, with a maximum percent error of 1.47% when comparing the case of no misalignment angle to the non-zero misalignment angle cases, independent of the method used. The estimated undamped mode shapes of the rotating blade with a large misalignment angle calculated using the novel misalignment angle correction method showed that there is good agreement with the undamped mode shapes of the rotating blade with no misalignment angle.

In addition to the presented results, this study highlights several key aspects of the proposed misalignment angle correction method. One of the primary advantages is that the method enables accurate scan path generation for rotating structures with significant misalignment angles, without requiring additional physical markers or encoders. This makes it well-suited for non-invasive applications in real-world scenarios. However, limitations exist in terms of hardware constraints, such as the field of view of the camera and the working distance of the LDV. While the method itself is theoretically applicable to misalignment angles of greater than 30°, practical implementation beyond this range would require more advanced imaging hardware and tracking algorithms. These findings suggest that the method has strong potential for application in full-scale rotating systems, provided that environmental and optical conditions are properly managed.

Acknowledgments This research was supported by the National Science Foundation through Grant No. CMMI-1763024.

References

1. S. Rothberg, M. Allen, and P. Castellini, An international review of laser Doppler vibrometry: making light work of vibration measurement, *Opt. Lasers Eng.* 99(1) (2017), pp. 11–22.
2. B. Stoffregen, and A. Felske, Scanning laser Doppler vibration analysis system. *SAE Transactions*, 94(2) (1985), pp 934-940.
3. P. Castellini, M. Martarelli, and E. Tomasini, Laser Doppler vibrometry: development of advanced solutions answering to technology's needs. *Mech. Syst. Signal Process*. 20(6) (2006) pp. 1265–1285.
4. K. Yuan, and W. Zhu, Modeling of welded joints in a pyramidal truss sandwich panel using beam and shell finite elements. *J. Vib. Acoust*. 143 (4) (2021), p. 041002.
5. C. Vuye, S. Vanlanduit, F. Presezniak, G. Steenackers, P. Guillaume, Optical measurement of the dynamic strain field of a fan blade using a 3D scanning vibrometer. *Opt. Lasers Eng*. 49 (7) (2011), pp. 988-997.
6. P. Sriram, S. Hanagud, J. Craig, and N.M. Komerath, Scanning laser Doppler technique for velocity profile sensing on a moving surface, *Appl. Opt.* 29(16) (1990), pp. 2409-2417.
7. P. Sriram, S. Hanagud, and J. Craig, Mode shape measurement using a scanning laser Doppler vibrometer, *Int. J. Anal. Exp. Modal anal*. 7(3) (1992), pp. 169–178.
8. M.S. Allen, and M.W. Sracic, A new method for processing impact excited continuous-scan laser Doppler vibrometer measurements, *Mech. Syst. Signal Process.* 24(3) (2010), pp. 721–735.
9. D.M. Chen, Y.F. Xu, and W.D. Zhu, Damage identification of beams using a continuously scanning laser Doppler vibrometer system, *J. Vib. Acoust.* 138(5) (2016), p. 05011.
10. D.M. Chen, and W.D. Zhu, Investigation of three-dimensional vibration measurement by three scanning laser Doppler vibrometers in a continuously and synchronously scanning mode. *J. Sound Vib.*, 498 (2021), p. 115950.
11. K. Yuan, and W.D. Zhu, Estimation of modal parameters of a beam under random excitation using a novel 3D continuously scanning laser Doppler vibrometer system and an extended demodulation method, *Mech. Syst. Signal Process.* 155 (2021), p. 107606.
12. K. Yuan, and W.D. Zhu, In-plane operating deflection shape measurement of an aluminum plate using a three-dimensional continuously scanning laser Doppler vibrometer system, *Exp. Mech.*, 62 (2022), pp. 667–676.
13. K. Yuan, and W.D. Zhu, A novel general-purpose three-dimensional continuously scanning laser Doppler vibrometer system for full-field vibration measurement of a structure with a curved surface, *J. Sound Vib.*, 540 (2022), p. 117274.
14. K. Yuan, and W.D. Zhu, Identification of modal parameters of a model turbine blade with a curved surface under random excitation with a three-dimensional continuously scanning laser Doppler vibrometer system, *Measurement*, 2023, p. 112759.
15. A. Stanbridge, and D. Ewins, Modal testing using a scanning laser Doppler vibrometer, *Mech. Syst. Signal Process.* 13(2) (1999), pp. 255–270.
16. D. Di Maio, and D. Ewins, Continuous scan, a method for performing modal testing using meaningful measurement parameters; Part I, *Mech. Syst. Signal Process.* 25(8) (2011), pp. 3027–3042.
17. D.M. Chen, Y.F. Xu, and W.D. Zhu, Experimental investigation of notch-type damage identification with a curvature-based method by using a continuously scanning laser Doppler vibrometer system, *J. Nondestruct. Eval.* 36(2) (2017), p. 38.
18. D.M. Chen, Y.F. Xu, and W.D. Zhu, Identification of damage in plates using full-field measurement with a continuously scanning laser Doppler vibrometer system, *J. Sound Vib.* 422 (2018), pp. 542–567.
19. D.M. Chen, Y.F. Xu, and W.D. Zhu, Non-model-based identification of delamination in laminated composite plates using a continuously scanning laser Doppler vibrometer system. *J. Vib. Acoust.* 140(4) (2018), p. 041001.
20. D.M. Chen, Y.F. Xu, and W.D. Zhu, A comprehensive study on detection of hidden delamination damage in a composite plate using curvatures of operating deflection shapes, *J. Nondestruct. Eval.* 38 (2019), p. 54.
21. Z. Huang, and C. Zang, Damage Detection Using Modal Rotational Mode Shapes Obtained with a Uniform Rate CSLDV Measurement, *Appl. Sci.* 9(23) (2019), p. 4982.
22. L.F. Lyu, and W.D. Zhu, Operational modal analysis of a rotating structure subject to random excitation using a tracking continuously scanning laser Doppler vibrometer via an improved demodulation method, *J. Vib. Acoust.*, 144 (1) (2022), p. 011006.
23. L.F. Lyu, and W.D. Zhu, Full-field mode shape estimation of a rotating structure subject to random excitation using a tracking continuously scanning laser Doppler vibrometer via a two-dimensional scan scheme, *Mech. Syst. Signal Process.* 169 (2022), p. 108532.

24. S., Yang, and M.S., Allen, Lifting approach to simplify output-only continuous-scan laser vibrometry, *Mech. Syst. Signal Process.* 45(2) (2014), pp. 267–282.
25. Y.F. Xu, D.M. Chen, and W.D. Zhu, Operational modal analysis using lifted continuously scanning laser Doppler vibrometer measurements and its application to baseline-free structural damage identification, *J. Vib. Control.* 25(7) (2019), pp. 1341-1364.
26. L.F. Lyu, and W.D. Zhu, Operational modal analysis of a rotating structure under ambient excitation using a tracking continuously scanning laser Doppler vibrometer system, *Mech. Syst. Signal Process.*, 152 (2021), p. 107367.
27. L.F. Lyu, G.D. Higgins, and W.D. Zhu, Operational modal analysis of a rotating structure using image-based tracking continuously scanning laser Doppler vibrometry via a novel edge detection method, *J. Sound Vib.*, 525 (2022), p. 116797.
28. L.F. Lyu, G.D. Higgins, and W.D. Zhu, A novel robust edge detection method for full-field modal parameter estimation using an image-based tracking continuously scanning laser Doppler vibrometer system. *Mech. Syst. Signal Process*., 195 (2023), p. 110242.
29. L. Lyu, and W. Zhu, A novel image-based long-range continuously scanning laser doppler vibrometer for operational modal analysis of a rotating structure. *Res. Nondestruct. Eval.,* (2024), pp. 1-16.
30. C. Lu, S. Xia, M. Shao, and Y. Fu, Arc-support line segments revisited: An efficient high-quality ellipse detection. *IEEE Trans. Imag. Process.,* 29 (2019), pp. 768-781.